ACS APPLIED MATERIALS & INTERFACES

www.acsami.org

Research Article

Multifunctional Magnetic CuS/Gd_2O_3 Nanoparticles for Fluorescence/Magnetic Resonance Bimodal Imaging-Guided Photothermal-Intensified Chemodynamic Synergetic Therapy of Targeted Tumors

Minchuan Luo, Hiroshi Yukawa,* Kazuhide Sato, Makoto Tozawa, Masato Tokunaga, Tatsuya Kameyama, Tsukasa Torimoto, and Yoshinobu Baba*

Cite This: *ACS Appl. Mater. Interfaces* 2022, 14, 34365−34376

Read Online

ACCESS | Metrics & More | Article Recommendations | Supporting Information

ABSTRACT: Chemodynamic therapy (CDT), which consumes endogenous hydrogen peroxide (H_2O_2) to generate reactive oxygen species (ROS) and causes oxidative damage to tumor cells, shows tremendous promise for advanced cancer treatment. However, the rate of ROS generation based on the Fenton reaction is prone to being restricted by inadequate H_2O_2 and unattainable acidity in the hypoxic tumor microenvironment. We herein report a multifunctional nanoprobe (BCGCR) integrating bimodal imaging and photothermal-enhanced CDT of the targeted tumor, which is produced by covalent conjugation of bovine serum albumin-stabilized CuS/Gd_2O_3 nanoparticles (NPs) with the Cy5.5 fluorophore and the tumor-targeting ligand RGD. BCGCR exhibits intense near-infrared (NIR) fluorescence and acceptable r_1 relaxivity (~15.3 $mM^{-1}\ s^{-1}$) for both sensitive fluorescence imaging and high-spatial-resolution magnetic resonance imaging of tumors in living mice. Moreover, owing to the strong NIR absorbance from the internal CuS NPs, BCGCR can generate localized heat and displays a high photothermal conversion efficiency (30.3%) under 980 nm laser irradiation, which enables photothermal therapy and further intensifies ROS generation arising from the Cu-induced Fenton-like reaction for enhanced CDT. This synergetic effect shows such an excellent therapeutic efficacy that it can ablate xenografted tumors *in vivo*. We believe that this strategy will be beneficial to exploring other advanced nanomaterials for the clinical application of multimodal imaging-guided synergetic cancer therapies.

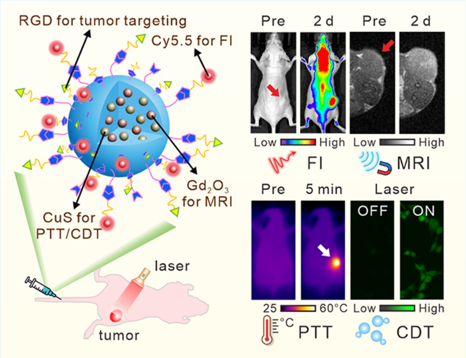

KEYWORDS: *copper sulfide, fluorescence imaging, magnetic resonance imaging, photothermal therapy, enhanced chemodynamic therapy*

INTRODUCTION

Worldwide, cancer has become a dominant cause of mortality. The induced generation of cytotoxic reactive oxygen species (ROS), such as superoxide ($\cdot O_2^-$), singlet oxygen ($^1O_2$), or hydroxyl ($\cdot OH$), which are capable of killing cancer cells by causing oxidative damage to intracellular biomolecules, has been exploited as a burgeoning cancer treatment strategy.[1−4] Photodynamic therapy (PDT), a type of light-triggered therapy, can convert oxygen into ROS, which is minimally invasive and highly selective, with low side effects compared with conventional therapies.[5] However, PDT suffers from limited penetration depth, and the ROS generation efficiency in the tumor microenvironment (TME) is low.[6−9] Different from PDT, chemodynamic therapy (CDT) is a continuous chemical process that converts H_2O_2 in the TME into toxic $\cdot OH$, which has also been validated as an effective tool for cancer treatment.[10−12]

Nowadays, CDT is generally based on Fenton or Fenton-like reactions, in which various nanomaterials are utilized as a catalyst to accelerate the disproportionation of H_2O_2 into oxidative $\cdot OH$. Fe^{2+}-based nanomaterials have been applied to tumor treatment, but they are not efficient enough in the weakly acidic TME (pH 6.5−6.9) because strong acidity (pH 2−4), which is required for the classic Fe^{2+}-guided Fenton reaction, is physiologically inaccessible.[13] In addition, the amount of ROS produced is largely limited by the low reaction rate (55 $M^{-1}\ s^{-1}$) even in an ideal pH condition.[13] In order to make the most of CDT that is appropriate for the weakly acidic TME, researchers have focused their attention on the development of other transition metal (Mn and Cu)-based nanomaterials for Fenton-like reactions.[11,12] Among these promising candidates, the cuprous ion (Cu^+) is an alternative

Received: April 13, 2022
Accepted: June 30, 2022
Published: July 25, 2022

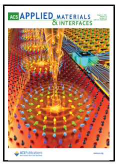

https://doi.org/10.1021/acsami.2c06503

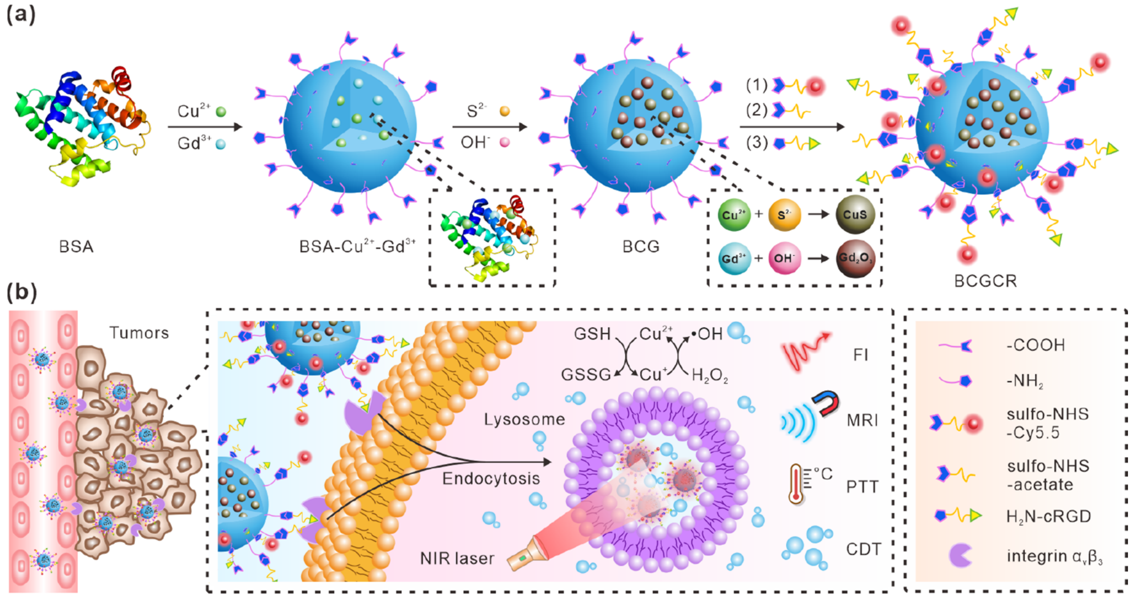

Figure 1. Schematic illustration of BCGCR. (a) Design. (b) Mechanisms of fluorescence/MR bimodal imaging-guided PTT and intensified CDT of targeted tumors.

due to the much higher reaction rate ($\sim 1 \times 10^4$ M^{-1} s^{-1}) and the feasibility of its application in weakly acidic and neutral media.[14] Nevertheless, the presence of sufficient endogenous biothiols (e.g., ~10 mM glutathione [GSH]) in cancer cells, which can scavenge the produced ·OH, restricts the efficiency of CDT. One strategy is to convert ample GSH into glutathione disulfide (GSSG) by the cupric ion (Cu^{2+}) via a redox reaction.[15−17] It is therefore essential to develop novel Cu^{2+}-based nanomaterials as a practicable and efficient CDT agent.

Copper chalcogenides are emerging as potential inorganic nanomaterials for this purpose. In particular, CuS nanoparticles (NPs), a kind of p-type semiconductor photosensitizer, possess strong and broad near-infrared (NIR) absorbance, high photothermal conversion efficiency (PCE), excellent photostability, and low toxicity.[18−22] These endow CuS NPs with a photothermal therapy (PTT) effect, which allows the thermal ablation of tumors by generating localized heat under NIR laser irradiation. This is noninvasive, provides deep penetration, and reduces damage to normal tissues.[23−26] Moreover, recent research on CuS nanomaterials has demonstrated that the hyperthermia caused by laser irradiation can promote Fenton-like reactions and accelerate the release of ROS, contributing to enhanced CDT of tumors.[27,28] This enables nanomaterial-mediated synergetic PTT and CDT for high-efficiency cancer treatment.

Basically, the preparation of CuS NPs was achieved in organic or aqueous phases. Organic syntheses are involved with high temperatures, toxic solvents, deoxygenated conditions, and the tedious phase transfer process before biological application.[20−22] It is preferable to propose a facile and moderate method for preparing CuS NPs for CDT-assisted PTT. In this study, we report the simultaneous production of versatile magnetic gadolinium oxide (Gd$_2$O$_3$) and CuS NPs through a simple one-pot synthesis method at room temperature and further decorate them into a fluorescent and tumor-targeting nanoprobe (BCGCR), which integrates NIR fluorescence/T_1-weighted MR bimodal imaging and NIR light-triggered PTT and enhanced CDT of tumors. Successful imaging and treatment of tumors in living mice suggest that this multifunctional nanomaterial has great prospects for application in progressive cancer theranostics in biomedical studies.

■ RESULTS AND DISCUSSION

Design and Characterization of BCGCR. The assembly of versatile BCGCR is illustrated in Figure 1a, including the preparation of bovine serum albumin (BSA)-capped CuS/Gd$_2$O$_3$ NPs (denoted as BCG) and subsequent decoration. BCG is produced using BSA as a template and stabilizer via a biomimetic mineralization according to the methods of previous reports, with some modification.[29,30] Cu^{2+} and Gd^{3+} are anchored in BSA to form a Cu^{2+}−BSA−Gd^{3+} complex based on the affinity between amino acid residues and metal ions. Then, OH$^-$ is introduced to adjust the pH (approaching 12), which induces BSA to extend into a hollow structure.[31] Afterward, CuS nanocrystals form and gradually grow following the addition of S^{2-}, while Gd^{3+} reacts with OH$^-$ to generate Gd$_2$O$_3$ NPs. The obtained BCG is further conjugated with a Cy5.5 fluorophore for NIR fluorescence with diminished scattering, absorption, and autofluorescence from the living organism, which is suitable for highly sensitive *in vivo* fluorescence imaging (FI).[32−36] Assisted by magnetic Gd$_2$O$_3$ NPs for magnetic resonance imaging (MRI), which provides high spatial resolution and unlimited penetrability,[37−40] this nanoprobe can be applied for dual-modality imaging to guide cancer treatment using an NIR laser. Then, sulfo-NHS-acetate was introduced to block −NH$_2$ of BSA to prevent self-polymerization in the subsequent peptide conjugation. The assembly of the RGD peptide facilitates active transport toward tumors since it has been accepted as a valid tumor-targeting ligand for selective recognition toward $\alpha_v\beta_3$ integrin overexpressed on the membrane of various tumor cells.[41,42]

Figure 1b depicts the mechanism of tumor detection and photoassisted treatment using BCGCR. Benefiting from the enhanced permeability and retention (EPR) effect, as well as $\alpha_v\beta_3$ integrin-mediated active recognition, BCGCR can partially arrive at tumors after intravenous administration and

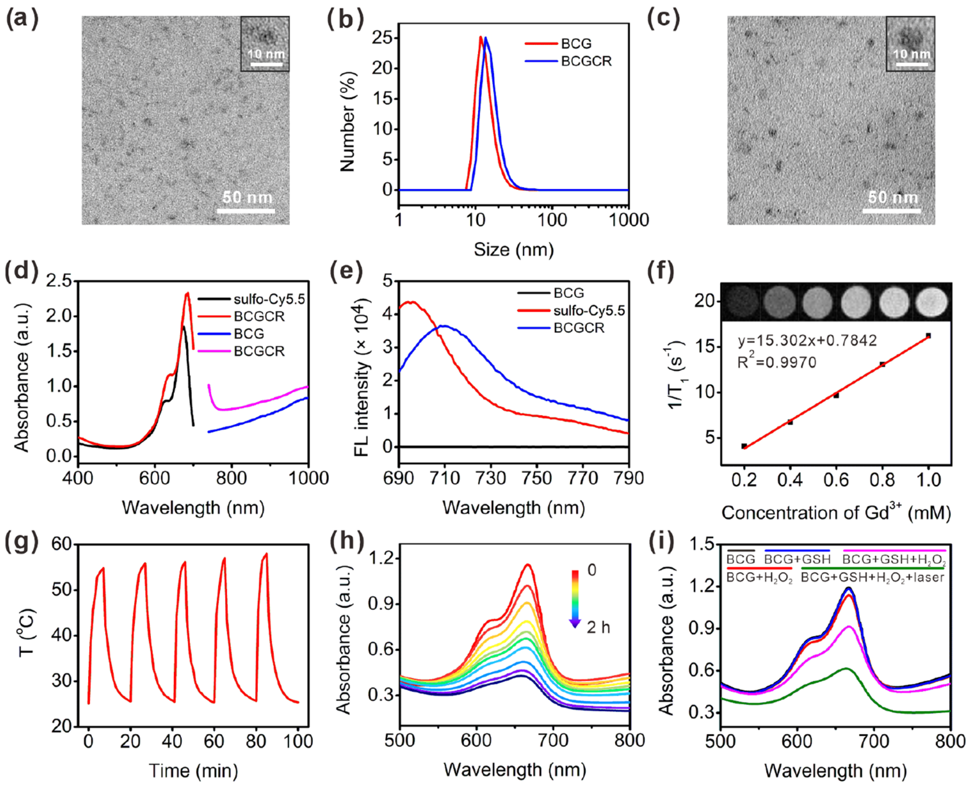

Figure 2. Characterization of BCG and BCGCR. (a) TEM image of BCG. (b) DLS analysis of BCG and BCGCR. (c) TEM image of BCGCR. (d) Absorption spectra of sulfo-Cy5.5 (0.1 mg/mL, black), BCGCR (2 mg/mL, red), BCG (20 mg/mL, blue), and BCGCR (25 mg/mL, pink). (e) Fluorescence (FL) spectra of BCG (10 mg/mL), sulfo-Cy5.5 (2 μg/mL), and BCGCR (1 mg/mL). λ_{ex} = 660 nm. (f) Plots of $1/T_1$ of BCGCR versus different Gd^{3+} concentrations from 0.2 to 1.0 mM. Inset: T_1-weighted MR images (1.5 T) of aqueous BCGCR with Gd^{3+} concentrations of 0, 0.2, 0.4, 0.6, 0.8, and 1.0 mM. TR/TE, 500/9.0 ms. (g) Photothermal stability of aqueous BCGCR (1 mM Cu^{2+}) for five cycles of heating by irradiation (980 nm, 0.8 W/cm^2) and natural cooling. (h) Absorption spectra of MB (10 μg/mL) incubated with BCG-GSH (0.5 mM Cu^{2+}) and H_2O_2 (20 μM) at pH 5.4 for 0, 3, 5, 10, 15, 20, 30, 60, 90, and 120 min. (i) Absorption spectra of (10 μg/mL) MB under different conditions at pH 5.4 with or without laser irradiation (980 nm, 0.8 W/cm^2) for 5 min.

preferentially accumulate into lysosomes by endocytosis. The process of BCGCR accumulation can be monitored in real time using both NIR FI from Cy5.5 fluorophores with an intense signal and tissue-penetrable MRI owing to the Gd element. Guided by the dual-mode imaging, the tumor site is exposed to NIR laser irradiation for treatment. The hyperthermia produced by internal CuS with high PCE ablates tumors and simultaneously accelerates the ionization of CuS. Then, the generation of ·OH is promoted by both hyperthermia and released Cu^{2+}, leading to the disintegration of cellular proteins and DNA. As a consequence, the synergistic PTT and enhanced CDT of tumors can be realized under guidance by bimodal imaging.

We first examined and ascertained the components of BCG. The X-ray photoelectron (XPS) spectrum of BCG in Figure S1 (see Supplementary Figures in the Supporting Information) includes several characteristic peaks attributed to O 1s, S 2p, Cu 2p, and Gd 4d, suggesting the existence of these elements. The composition of BCG was further verified by an energy-dispersive spectrometry (EDS) analysis with element line scanning data (Figure S2). The X-ray diffraction (XRD) pattern of BCG exhibited distinct peaks at 29.42 and 47.07° assigned to the characteristic peaks of both hexagonal CuS and cubic Gd_2O_3, indicating the successful preparation of these nanocrystals (Figure S3). Next, the BCG morphology was investigated by transmission electron microscopy (TEM), exhibiting a uniform spherical structure with an average size of 5 nm (Figure 2a), which was slightly smaller than the hydrodynamic size calculated by a dynamic light scattering (DLS) analysis (∼13 nm) (Figure 2b). In addition, it is obvious that the broad NIR absorption band from BCG was consistent with the one from Gd-free CuS NPs, indicating strong localized surface plasmon resonance (LSPR) from inner CuS nanocrystals (Figure S4).

Inspired by the successful preparation, we used the sulfo-NHS-Cy5.5 fluorophore and cRGDfk to decorate BCG into a multifunctional nanoprobe (BCGCR) (Figure S5). TEM indicates that BCGCR took on a similar morphology to BCG (Figure 2c). A DLS analysis shows that the average hydrodynamic size of BCGCR was approximately 16 nm (Figure 2b), which was slightly larger than that of BCG due to the introduction of sulfo-Cy5.5, acetyl amino groups, and cRGDfk. The zeta potential of BCGCR remained negative (−16.8 mV) in comparison to BCG (−13.9 mV) due to the negatively charged sulfo groups from sulfo-Cy5.5 and carboxyl groups from BSA and RGD (Figure S6). The absorption spectra illustrate that BCGCR inherited two characteristic absorption peaks (640 and 685 nm) from sulfo-Cy5.5 and strong NIR absorbance (700−1000 nm) from CuS NPs (Figure 2d). In order to assess the ability of BCGCR as a bimodal imaging agent, we first measured the fluorescence signal. As depicted in Figure 2e, the fluorescence spectrum of BCGCR resembled that of sulfo-Cy5.5, exhibiting strong NIR fluorescence around 710 nm, which showed great potential for

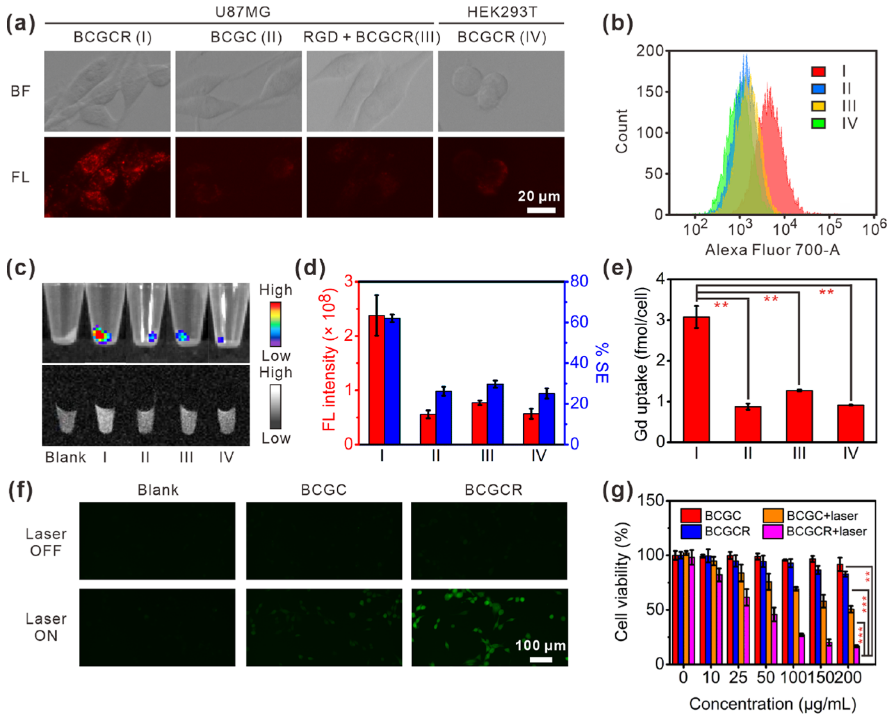

Figure 3. *In vitro* bimodal imaging of cells, CDT performance, and cytotoxicity studies. (a) Fluorescence images of (I) U87MG cells incubated with BCGCR (100 μg/mL, 2 h), (II) U87MG cells incubated with BCGC (100 μg/mL, 2 h), (III) U87MG cells incubated with RGD (10 μM, 1 h) followed by BCGCR (100 μg/mL, 2 h), or (IV) HEK293T cells incubated with BCGCR (100 μg/mL, 2 h) (ex: 650 ± 22 nm, em: 720 ± 30 nm). (b) Flow cytometry assays of fluorescence intensity in cells after similar treatments with BCGC or BCGCR (10 μg/mL) for 2 h (ex: 633 nm, em: 710 ± 25 nm). (c) Fluorescence (top) (ex/em. = 675/720 nm) images of cell pellets after similar treatments with BCGC or BCGCR (10 μg/mL) for 2 h and T_1-weighted MR (bottom) (TR/TE = 500/9.0 ms at 1.5 T) images of cell pellets after similar treatments with BCGC or BCGCR (10 μM Gd^{3+}) for 24 h. (d) Statistics of total FL intensities (red) and average % MR signal enhancements (% SE, blue) of cell pellets in (c). (e) ICP-AES analysis of the average Gd uptake in each cell after indicated treatments in (c, bottom). (f) Fluorescence images of U87MG cells (untreated, incubated with 100 μg/mL BCGC or BCGCR, 6 h) followed by 10 μM DCFH-DA staining with or without laser irradiation (980 nm, 0.8 W/cm^2) for 5 min (ex: 470 ± 20 nm, em: 525 ± 25 nm). (g) U87MG cell viability after incubation with different concentrations of BCGC or BCGCR for 24 h followed by exposure (or nonexposure) to laser irradiation (980 nm, 0.8 W/cm^2) for 5 min. Values denote the mean ± SD ($n = 5$ for cell viability and $n = 3$ for others; $^{**}P < 0.01$, $^{***}P < 0.001$).

in vivo FI. The redshift of BCGCR fluorescence after modification probably resulted from the change in the chemical environment around the sulfo-Cy5.5 fluorophore. It was also found that the brightness of T_1-weighted MR images was amplified with the concentration of BCGCR, and the longitudinal relaxivity (r_1) was calculated to be ~15.3 mM^{-1} s^{-1} per Gd^{3+} in aqueous solution (Figure 2f), almost 4 times as high as that of the clinical paramagnetic contrast agent Gd-DOTA (3.4 mM^{-1} s^{-1}).[43] The elevated r_1 relaxivity probably arose from the spatial confinement of encapsulated Gd within BSA, which impeded rotation and prolonged the tumbling time (τ_R).[44,45] Moreover, BCGCR was stable in three different types of solutions without any size change for at least one week (Figure S7). Based on these results, BCGCR is expected to have applications as both a fluorescent nanoprobe and an effective T_1-weighted MR contrast agent for dual-modal imaging.

Evaluation of the Photothermal Effect and Catalytic Performance. We next evaluated the photothermal performance by irradiation with a 980 nm laser. As shown in Figure S8, the solution temperature exhibited a positive correlation with both the BCGCR concentration and the laser power density. For instance, after 5 min of irradiation with a power density of 0.8 W/cm^2, the IR thermal image of the BCGCR solution (0.5 mM Cu^{2+}) gradually became bright and its temperature dramatically increased from 25.3 to 50.6 °C, whereas a negligible temperature increase was observed in ultrapure water. The PCE (η) of BCGCR was calculated to be 30.3% (Figure S9 and Note S1), which was comparable with that of previously reported CuS NPs (Table S1). In addition, BCGCR possessed excellent photothermal stability for at least five cycles of heating by irradiation and subsequent natural cooling, indicating great potential for application in PTT of tumors (Figure 2g).

To investigate the Fenton-like catalytic efficiency of BCGCR, methylene blue (MB), which can be degraded by ·OH and gives rise to decreased absorbance, was selected as an indicator to reflect the ·OH generation level.[11,15] As the absorbance of Cy5.5 from BCGCR overlapped and probably interfered with that of MB, BCG rather than BCGCR was used to evaluate ·OH production. Figure 2h shows that MB gradually faded under the condition of H_2O_2, BCG, and GSH, suggesting that the generation of ·OH was induced by the Fenton-like reaction. In comparison, MB absorbance almost remained constant after incubation with BCG, BCG + GSH, or BCG + H_2O_2 (Figure 2i). Without the help of Cu, it was difficult for MB degradation to proceed (Figure S10). This Cu-triggered Fenton-like reaction could smoothly proceed at varying pH values of 5.4 simulating the weak acidity in lysosomes, 6.4 as the TME, and 7.4 as the physiological environment (Figure S11). In order to verify the photothermal-intensified ·OH generation, we assumed 50 °C as the

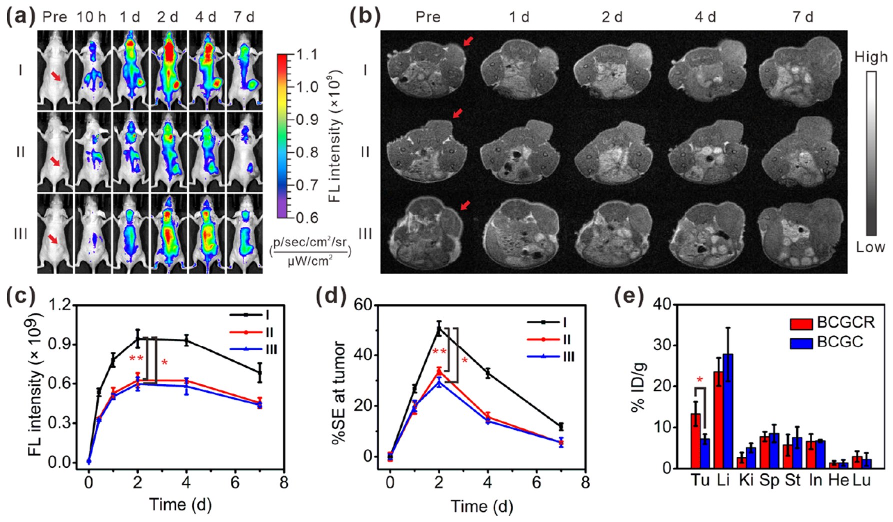

Figure 4. Bimodal imaging of U87MG tumors in living mice as well as biodistribution analysis. (a) FL images of mice receiving (I) i.v. injection of BCGCR (5 mg/kg, 100 μL), (II) i.t. injection of free cRGDfk (2 mM, 100 μL) followed by i.v. injection of BCGCR (5 mg/kg, 100 μL) 1 h later, and (III) i.v. injection of BCGC (5 mg/kg, 100 μL) at 0 h, 10 h, 1 day, 2 days, 4 days, and 7 days (ex: 675 nm, em: 720 nm). (b) T_1-weighted MR images of mice receiving (I) i.v. injection of BCGCR (20 μmol/kg Gd^{3+}, 200 μL), (II) i.t. injection of free cRGDfk (2 mM, 100 μL) followed by i.v. injection of BCGCR (20 μmol/kg Gd^{3+}, 200 μL) 1 h later, and (III) i.v. injection of BCGC (20 μmol/kg Gd^{3+}, 200 μL) at 0 h, 1 day, 2 days, 4 days, and 7 days (TR/TE = 500/9.0 ms at 1.5 T). Red arrows indicate the tumor locations in mice. (c) Variations of average FL intensity at the tumor with time in (a). (d) Variations of average % SE at the tumor with time in (b). (e) Biodistribution (% ID/g) of BCGCR (red) or BCGC (blue) in the main organs and the U87MG tumor (Tu: tumor; Li: liver; Ki: kidneys; Sp: spleen; St: stomach; In: intestines; He: heart; Lu: lungs) at 2 days after i.v. injection of BCGC (10 mg/kg Cu^{2+}) or BCGCR (10 mg/kg Cu^{2+}) determined via a quantification analysis of the amount of Cu^{2+} by ICP-AES. Values denote the mean ± SD ($n = 3$, $^*P < 0.05$, and $^{**}P < 0.01$).

temperature that could be reached for PTT, and rapid MB degradation was observed at high temperatures (Figure S11). Correspondingly, MB degradation was strengthened with the help of laser irradiation (Figure 2i). These data suggest the potential application of BCG (or BCGCR) as an efficient photothermal-enhanced CDT agent for cancer theranostics.

***In Vitro* Bimodal Imaging Performance.** Prompted by the abovementioned characteristics, we used $\alpha_v\beta_3$ integrin-positive U87MG tumor cells to investigate its effects on *in vitro* fluorescence/MR bimodal imaging.[46,47] Fluorescence images reveal that NIR fluorescence inside U87MG cells became bright with incubation time (Figure S12). The effective uptake of BCGCR by U87MG cells was confirmed by a set of confocal fluorescence images at different depths (Figure S13). It was further proven by a colocalization study with the help of a lysosomal tracker that intracellular flecky fluorescence was principally located at the lysosomes (Figure S14). In contrast, weak fluorescence was found in (II) U87MG cells incubated with RGD-free BCGC, (III) U87MG cells pretreated with RGD followed by incubation with BCGCR, or (IV) $\alpha_v\beta_3$ integrin-negative HEK293T cells incubated with BCGCR (Figure 3a). Flow cytometry showed that the fluorescence intensity in U87MG cells incubated with BCGCR was remarkably stronger in comparison to the other three abovementioned groups (Figure 3b). The bright NIR fluorescence from BCGCR-treated U87MG cells was also observed against that from other groups (almost 4-fold) by FI of cell pellets (Figure 3c, top and Figure 3d, red), which is well-correlated with the abovementioned results.

Along with the strong intracellular fluorescence, T_1-weighted MR brightness was enhanced in U87MG cells incubated with BCGCR (Figure 3c, bottom). The percentage signal enhancement (% SE) against untreated U87MG cell pellets was ~62.0%, which was higher than that of U87MG cells incubated with BCGC (26.2%), U87MG cells pretreated with RGD followed by incubation with BCGCR (29.7%), and HEK293T cells incubated with BCGCR (25.1%) (Figure 3d, blue). An ICP-AES analysis that was performed to investigate the uptake of Gd by cells demonstrates a large amount of intracellular Gd (~3.1 fmol/cell) in U87MG cells incubated with BCGCR against that from other groups (Figure 3e). These findings imply that $\alpha_v\beta_3$ integrin overexpressed on the membrane of U87MG cells played a significant role in active recognition and subsequent uptake, leading to strong intracellular NIR fluorescence intensity and MR contrast for *in vitro* bimodal imaging.

***In Vitro* Synergetic PTT and Enhanced CDT Evaluation.** To investigate the *in vitro* anticancer efficacy of BCGCR under NIR irradiation, we first assessed the feasibility of CDT. A GSH assay kit was applied to monitor the intracellular GSH level. A large quantity of GSH in U87MG cells was consumed after treatment with BCGCR, suggesting the conversion from Cu^{2+} to Cu^+ for the subsequent Fenton-like reaction (Figure S15). Then, we evaluated the intracellular ROS generation with monitoring by 2,7-dichlorodihydrofluorescein diacetate (DCFH-DA), which is able to be oxidized into DCF with green fluorescence emission.[48] As described in Figure 3f, green fluorescence could not be observed on U87MG cells treated with either BCGC or BCGCR without laser irradiation, indicating little intracellular ROS generation. Once exposed to laser irradiation, the ROS produced by U87MG cells incubated with BCGCR was dramatically enhanced, which demonstrates the photothermal-intensified Fenton-like reaction. In comparison, weak fluorescence was found on U87MG cells treated with BCGC, even if exposed to laser irradiation due to the limited uptake.

Before applying BCGCR to photoassisted therapies of *in vitro* U87MG cells, we investigated its cytotoxicity toward

https://doi.org/10.1021/acsami.2c06503
ACS Appl. Mater. Interfaces 2022, 14, 34365−34376

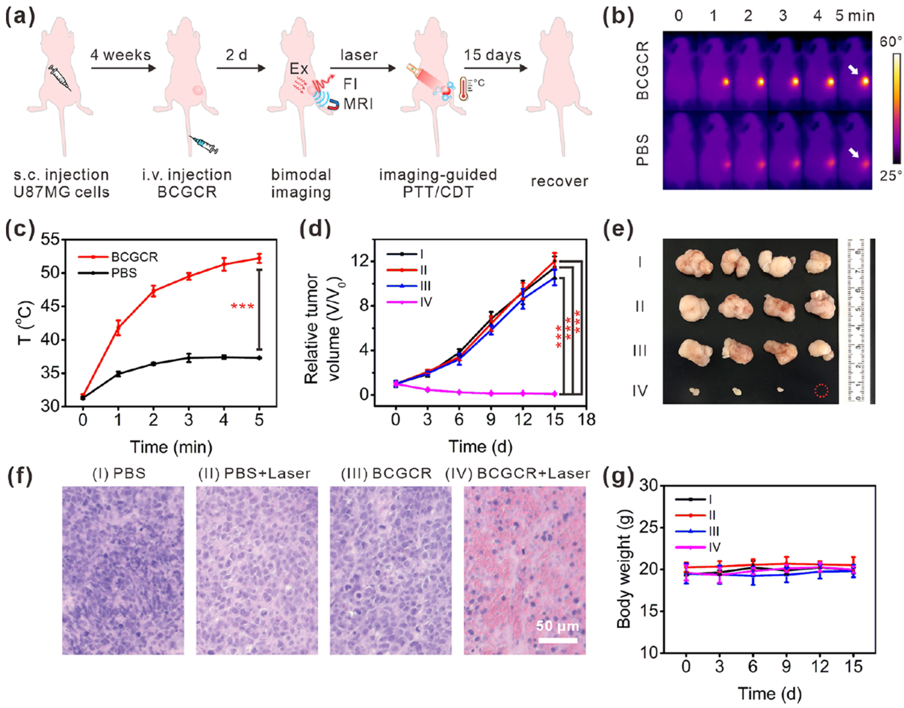

Figure 5. Synergetic PTT and intensified CDT of tumors *in vivo*. (a) Schematic illustration of the process of fluorescence/MR bimodal imaging-guided synergetic PTT/CDT of U87MG tumors in living mice. (b) IR thermal images of U87MG tumors in living mice during exposure to 980 nm laser irradiation (0.8 W/cm^2) for 0−5 min at 2 days after i.v. injection of PBS (200 μL) or BCGCR (5 mg/kg Cu^{2+}, 200 μL). White arrows indicate the tumor locations in mice. (c) Average temperature variations of the tumor with time in (b). (d) Relative tumor volume variation in living mice with time after treatments with (I) PBS (200 μL), (II) PBS (200 μL) + laser (0.8 W/cm^2, 10 min), (III) BCGCR (5 mg/kg Cu^{2+}, 200 μL), and (IV) BCGCR (5 mg/kg Cu^{2+}, 200 μL) + laser (0.8 W/cm^2, 10 min). (e) Photograph of tumors resected from mice on the 15th day after the indicated treatments. (f) H&E staining of U87MG tumor slices resected from mice on the second day after indicated treatments. (g) Average body weight variation of mice with time after the indicated treatments. Values denote the mean ± SD ($n = 4$, $^{***}P < 0.001$).

normal HEK293T cells via a cytotoxicity assay (CCK-8). Figure S16 suggests that BCGCR had no influence on cell viability toward HEK293T cells, indicating excellent biocompatibility for cell studies. Then, we tried to examine the PTT/CDT efficacy of BCGCR against U87MG cells. Figure 3g shows that BCGC and BCGCR had negligible cytotoxicity against U87MG cells without laser irradiation, at concentrations of up to 200 μg/mL. However, it is suggested that the cell viability was negatively correlated with dosage upon laser irradiation (0.8 W/cm^2) for 5 min. In detail, the relative cell viability declined to ∼27.0% for 100 μg/mL BCGCR-treated U87MG cells exposed to laser irradiation, which was remarkably lower than that for 100 μg/mL BCGC-treated U87MG cells (∼69.2%). Cell death caused by the synergistic PTT and CDT was further demonstrated by fluorescence staining of U87MG cells via calcein AM (live) and propidium iodide (PI) (dead) (Figure S17). These results demonstrate that BCGCR had the potential to ablate *in vitro* U87MG tumor cells under laser irradiation by CDT-assisted PTT.

***In Vivo* Tumor-Targeted Bimodal Imaging Performance.** We then applied BCGCR to the detection of U87MG tumor xenografts in living mice via NIR fluorescence and MR dual-modal imaging. Figure 4a indicates that after the intravenous (i.v.) injection of BCGCR (5 mg/kg, 100 μL), fluorescence at U87MG tumors gradually augmented, which peaked at 2 days and lasted for at least one week. This strong fluorescence at tumors could be effectively reduced by intratumoral (i.t.) injection of free cRGDfk (∼1.51-fold lower) due to the lack of RGD-mediated active transport (Figure 4c). In addition, an ∼1.58-fold decrease in fluorescence intensity at the tumor was observed in mice that received i.v. injection of BCGC compared with those treated with BCGCR. These apparent differences in fluorescence intensity were further confirmed by the FI of tumor tissue slices resected from mice at 2 days after i.v. injection (Figure S18). In accordance with the FI findings, the T_1-weighted MR contrast of the U87MG tumor gradually intensified until 2 days after i.v. injection of BCGCR (20 μmol/kg Gd^{3+}, 200 μL) (Figure 4b). The maximum signal enhancement (% SE) of the tumor was ∼50.8% at 2 days, which was nearly 1.50-fold as high as that with blocking by RGD and 1.73-fold higher than that with BCGC treatment (Figure 4d). This enhanced brightness could be observed throughout the entire tumor tissue on a set of multislice MR images, suggesting the superb tissue penetrability of BCGCR (Figure S19).

The biodistribution of BCGC and BCGCR was then investigated by *ex vivo* FI of the main organs and tumors resected from mice. Figure S20 shows that at 2 days after i.v. injection, BCGCR-treated tumors exhibited strong fluorescence, which was almost 2.04-fold higher than that of BCGC-treated ones, although most fluorescence was distributed in the liver in both groups. Furthermore, an accurate biodistribution study by ICP-AES reveals that the % ID/g of BCGCR-treated tumors was ∼13.3%, which was higher than that of other major organs, with the exception of the liver and BCGC-treated tumors (∼7.2%) (Figure 4e). Such a high uptake of BCGCR benefited from RGD-induced active recognition assisted by the EPR effect. These findings correspond to strong fluorescence and intensified MR contrast at the tumor, as monitored by real-time imaging of living mice, demonstrating that BCGCR could be efficiently accumulated in U87MG tumors *in vivo* and could act as a sensitive fluorescence probe and MR contrast agent for bimodal imaging.

***In Vivo* Synergetic PTT and Enhanced CDT of Tumor Xenografts.** Guided by precise fluorescence/MR bimodal imaging, synergetic PTT and enhanced CDT of U87MG tumors were conducted in living mice that received the i.v. injection of PBS (200 μL) or BCGCR (5 mg/kg Cu^{2+}, 200 μL) followed by exposure (or nonexposure) to 980 nm laser irradiation (0.8 W/cm^2) for 10 min when the accumulation of BCGCR in the tumor peaked (2 days later) (Figure 5a). Real-time thermal images, as well as the corresponding temperature variation of the tumors, were recorded using an infrared (IR) thermal camera (Figure 5b,c). It is clear that the tumor temperature in BCGCR-treated mice was promptly enhanced from ~31.7 to ~51.8 °C after laser irradiation for 5 min, which was higher than that in PBS-treated mice (~37.3 °C). This hyperthermia could cause tremendous damage to tumor tissues in living mice.

We finally evaluated the curative efficacy after the indicated treatments. By measuring the tumor volumes within 15 days after treatment, we found that the tumor growth was successfully inhibited in the case of BCGCR-treated mice followed by laser irradiation, whereas tumor volumes from other groups (I−III) still expanded rapidly (Figure 5d). We verified, using a photograph of tumors dissected on the 15th day, that after BCGCR plus laser treatment, tumors were much smaller in comparison to the control groups (Figure 5e). A histopathological study by hematoxylin and eosin (H&E) staining of tumor tissue slices on the second day after treatment implies that BCGCR plus laser treatment induced tumor necrosis relative to the other three groups (Figure 5f). The dose and laser output required for this therapeutic effect were similar to those from previous reports, indicating the potential application of CuS NPs as a photoassisted tumor therapy agent (Table S2).

To assess the *in vivo* toxicity, H&E staining of tissue slices of major resected organs (heart, lungs, liver, spleen, and kidneys) was conducted at the end of each treatment, which reveals no apparent pathological variation (Figure S21). The hematological assay of mice at 15 days postinjection indicates negligible differences between BCGCR-treated mice and PBS-treated ones (Figure S22). Moreover, there was no distinct change in the body weight of mice among these four groups after each treatment (Figure 5g). These results demonstrate that BCGCR featured synergetic PTT and intensified CDT against U87MG tumors *in vivo*, as well as excellent biocompatibility in living mice.

CONCLUSIONS

In summary, a multifunctional tumor-targeted nanoprobe (BCGCR) was developed by embellishing BSA-capped magnetic semiconductor CuS/Gd_2O_3 NPs, and we demonstrated the feasibility of fluorescence/MR bimodal imaging-guided synergetic PTT and intensified CDT of tumors in living mice. The as-prepared BCGCR exhibited intense NIR fluorescence and satisfactory r_1 relaxivity, permitting *in vivo* bimodal imaging of tumors with high sensitivity and spatial resolution. Furthermore, BCGCR possessed a high PCE (30.3%) under 980 nm laser irradiation, which could effectively generate hyperthermia to ablate tumors. On the other hand, a Cu-induced Fenton-like reaction was also promoted to produce abundant ROS in the hyperthermal TME, resulting in oxidative damage to tumors. As a result of this synergistic effect, tumor xenografts in mice were eliminated under guidance by imaging. This study reveals the ability of BCGCR for dual-modality imaging and PTT assisted with enhanced CDT of U87MG tumors, which may also be applicable to other malignant tumors as a precise theranostic agent. This strategy is expected to be adopted in the design of other nanoprobes for multimodal imaging, as well as in synergetic therapies for advanced cancer theranostics.

EXPERIMENTAL METHODS

Chemicals and Reagents. Copper(II) chloride dihydrate ($CuCl_2{\cdot}2H_2O$), gadolinium(III) chloride hexahydrate ($GdCl_3{\cdot}6H_2O$), sodium hydroxide (NaOH), bovine serum albumin, sodium sulfide pentahydrate ($Na_2S{\cdot}5H_2O$), methylene blue, and Hoechst 33342 solution were purchased from Fujifilm Wako Pure Chemical Co. (Osaka, Japan). Sulfo-NHS-Cy5.5 ester was obtained from Abcam (Cambridge, UK). Cyclo(RGDfk) and 2,7-dichlorodihydrofluorescein diacetate (DCFH-DA) were obtained from Cayman Chemical (Michigan, USA). Sulfo-NHS-acetate was purchased from BroadPharm, California (USA). 1-Ethyl-3-(3-dimethylaminopropyl)-carbodiimide hydrochloride (EDC), *N*-hydroxysulfosuccinimide (sulfo-NHS), Alexa Fluor 488 phalloidin, LysoTracker Green DND-26, calcein AM, and propidium iodide (PI) were obtained from Thermo Fisher Scientific (Massachusetts, USA). All other chemicals of analytical reagent grade were obtained from qualified reagent suppliers.

Instruments and Apparatuses. XPS spectra were recorded on an ESCALAB250 system with Al Kα as an X-ray source (Thermo Scientific, America). EDS line scanning results were obtained using an SU-1500 scanning electron microscope (Hitachi, Japan) with an EMAX X-ray spectrometer (Horiba, Japan). X-ray powder diffraction (XRD) patterns were obtained on a SmartLab X-ray diffractometer (Rigaku, Japan). TEM images were obtained by an H-7650 transmission electron microscope (Hitachi, Japan) with an accelerating voltage of 100 kV. DLS and the zeta potential analysis were performed using a Malvern Zetasizer ZEN3600 (Malvern Instruments Ltd., UK). Cu^{2+} and Gd^{3+} concentrations were measured using an SPS7800 inductively coupled plasma-atomic emission spectrometer (ICP-AES) (Seiko Instruments, Inc., Japan). An Infinite 200 Pro microplate reader (Tecan, Austria) was used for UV−vis−NIR absorption spectra and fluorescence spectra scanning. Fluorescence images of cells were acquired using a BZ-X700 all-in-one fluorescence microscope (Keyence, Japan) or an A1RMP multiphoton confocal laser scanning microscope (Nikon, Japan). Flow cytometry assays were conducted using a BD LSRFortessa X-20 flow cytometer (BD Biosciences, America). *In vitro*/*in vivo* MR imaging was acquired using a 1.5 ± 0.1 T MR VivoLVA 1506 MRI system (Japan REDOX, Japan). Whole-body fluorescence images were acquired using an IVIS Spectrum CT system (PerkinElmer, America). A 980 nm NIR laser (Shanghai Dream Lasers Technology Co., Ltd., China) was used to evaluate the photothermal effect and for *in vitro*/*in vivo* PTT/CDT experiments. Thermal images with real-time temperature were recorded using an FLIR C2 IR thermal camera (FLIR Systems, Inc., America).

Synthesis of BSA-Stabilized CuS/Gd_2O_3 (BCG). BCG was produced by biomineralization according to previously reported methods, with modification.[29,30] Briefly, 200 mg of BSA was dispersed in 7 mL of H_2O by ultrasound followed by the addition of 1 mL of 40 mM $CuCl_2{\cdot}2H_2O$ and 1 mL of 20 mM $GdCl_3{\cdot}6H_2O$ under continuous stirring. After 2 min, 0.4 mL of 1 M NaOH was used to adjust the pH of the mixture to ~12, and 0.16 mL of 1 M $Na_2S{\cdot}5H_2O$ was subsequently added. The colloid mixture was further stirred in the dark for another 5 h at room temperature followed by dialysis (MWCO = 10 K) for 24 h via ultrapure water to remove unreacted ions. Finally, the deep-brown mixture was stored at 4 °C in the dark for further modification.

Modification of BCG with Cy5.5 and RGD. For modification of Cy5.5 with BCG, 0.1 mL of PBS (pH 7.2, 10×) and 0.5 mg of sulfo-NHS-Cy5.5 were added to 0.9 mL of BCG containing 10 mg of BSA, and the mixture was stirred in dark conditions overnight. Sulfo-NHS-acetate (10 mg) was added and stirred for another 2 h to block residual $-NH_2$ groups of BSA. The unreacted sulfo-NHS-Cy5.5 and sulfo-NHS-acetate were removed by ultrafiltration (30 kDa, 3000 g, Millipore) via PBS (pH 7.2, 1×), and Cy5.5-conjugated BCG was obtained (denoted as BCGC). In order to further conjugate the tumor-targeting peptide (RGD), 2 mg of EDC was added to the prepared mixture and stirred for 15 min. Subsequently, 2 mg of sulfo-NHS was added and allowed for another 1 h reaction to activate carboxyl groups followed by addition of 0.9 mg of cRGDfk. The reaction was left overnight, and the mixture was purified by ultrafiltration (30 kDa, 3000 g) via PBS (pH 7.2, 1×). The obtained BCGCR NPs were resuspended in PBS and stored at 4 °C in the dark for application. The concentrations of Gd and Cu in the prepared mixture were determined by ICP-AES.

Photothermal Effect Evaluation. BCGCR (0, 0.125, 0.25, 0.5, and 1 mM Cu^{2+}) in 0.3 mL of PBS was added to a 48-well plate followed by irradiation with a 980 nm laser at a power density of 0.8 W/cm^2 for 5 min. BCGCR (0.5 mM Cu^{2+}) in 0.3 mL of PBS was irradiated with various power densities (0, 0.2, 0.5, 0.8, and 1.0 W/cm^2) for 5 min. For temperature quantification, thermal images were recorded every 1 min using an IR thermal camera.

To evaluate the photothermal conversion efficiency, BCGCR (1 mM Cu^{2+}) in 0.3 mL of PBS was added into a 48-well plate followed by irradiation with a 980 nm laser at a power density 0.8 W/cm^2 for 7 min. Thermal images with temperature quantification were recorded every 1 min using an IR thermal camera, which captured the whole processes of both the temperature increase and subsequent natural cooling.

Measurement of ·OH Generation. BCG (10 mg/mL) was mixed with 1 mM GSH solution for 30 min to obtain the intermediate product BCG-GSH. The obtained BCG-GSH (0.5 mM Cu^{2+}) was mixed with 10 μg/mL MB and 20 mM H_2O_2 at different pH values (5.4, 6.4, or 7.4) at different temperatures. To investigate the enhanced ·OH generation under irradiation, BCG-GSH (0.5 mM Cu^{2+}) was mixed with 10 μg/mL MB and 20 mM H_2O_2 at pH 5.4 followed by laser irradiation (0.8 W/cm^2) for 5 min. In addition, BCG, BCG + GSH (1 mM), BCG + H_2O_2, and BCG + GSH + H_2O_2 at the same concentration were mixed with 10 μg/mL MB for 5 min as a control group. The ·OH generation was evaluated according to MB degradation, which was measured via the absorbance decrease on a microplate reader.

Cell Culture. Human glioma U87MG cells and human embryonic kidney HEK293T cells were cultured in DMEM (Gibco) medium with 10% fetal bovine serum (FBS) (v/v %) and 1% penicillin/streptomycin (PS) (v/v %) in a cell incubator with 5% CO_2 at 37 °C. PBS (pH 7.2, 1×) and 0.25% (m/v %) trypsin with 0.1% (m/v %) EDTA·4Na were used for cell rinsing and digestion, respectively.

FI of Cells. To obtain time-dependent fluorescence images, U87MG cells (~2 × 10^4) were seeded in a 48-well plate and allowed to grow for 24 h. BCGCR (100 μg/mL) in 0.25 mL of DMEM medium was added to U87MG cells and incubated for 1, 2, 3, 4, and 6 h. Then, the solution was removed and rinsed with PBS twice.

To verify $\alpha_v\beta_3$ integrin-mediated active delivery, U87MG and HEK293T cells (~2 × 10^4) were seeded in a 48-well plate and allowed to grow for 24 h. BCGCR (100 μg/mL) in 0.25 mL of DMEM medium was added to U87MG and HEK293T cells. In addition, RGD-free BCGC (100 μg/mL) and RGD + BCGCR (100 μg/mL, pretreated with 10 μM cRGDfk for 1 h to block $\alpha_v\beta_3$ integrin) in 0.25 mL of DMEM medium were added to U87MG cells. After incubation for 2 h, the solution was removed and rinsed with PBS twice.

Finally, fluorescence images were acquired using a fluorescence microscope through a Cy5.5 filter (ex: 650 ± 22 nm, em: 720 ± 30 nm).

Internalization Analysis. U87MG cells (~1 × 10^5) were seeded in a 35 mm glass-bottom dish and allowed to grow for 24 h. BCGCR (50 μg/mL) in 1.0 mL of DMEM medium was added and incubated for 2 h. After that, the solution was removed and rinsed by PBS once followed by fixing with 4% polyfluoroalkoxy (PFA). These cells were then costained using 0.1 μg/mL Hoechst 33342 and 300 nM Alexa Fluor 488 phalloidin for another 30 min and rinsed with PBS twice.

To examine the intracellular location further, BCGCR-treated U87MG cells (mentioned above) were subsequently costained with 0.1 μg/mL Hoechst 33342 and 200 nM LysoTracker (LysoTracker Green) for 20 min. These cells were rinsed with PBS twice, and fresh DMEM medium was added.

Finally, fluorescence images were acquired using a confocal laser scanning microscope through the DAPI channel (ex: 402.5 nm, em: 450 ± 25 nm) for Hoechst 33342, the Alexa 488 antibody channel (ex: 487.8 nm, em: 525 ± 25 nm) for Alexa Fluor 488 phalloidin or LysoTracker Green, and the Cy5.5 channel (ex: 639.8 nm, em: 700 ± 37 nm) for BCGCR.

Flow Cytometry. U87MG cells and HEK293T cells (~2 × 10^5) were seeded in 6-well plates and allowed to grow for 24 h. BCGCR (10 μg/mL) in 2 mL of DMEM medium was added to U87MG and HEK293T cells. In addition, RGD-free BCGC (10 μg/mL) and RGD + BCGCR (10 μg/mL, pretreated with 10 μM cRGDfk for 1 h to block $\alpha_v\beta_3$ integrin) in 2 mL of DMEM medium were added to U87MG cells. After incubation for 2 h, the solution was removed, and these cells were rinsed by PBS once. To detach these cells, 0.5 mL of trypsin was added into each well and kept for 2 min followed by addition of 0.5 mL of culture medium to stop digestion. These cells were transferred into 1.5 mL tubes and collected by centrifugation (1500 rpm) for 5 min. After discarding the supernatants, dispersing by 1 mL of PBS, and centrifuging (1500 rpm) for 5 min again, these cells were resuspended by 0.5 mL of FACS buffer (PBS with 1% BSA and 0.1% NaN_3) and filtered through 70 μm cell strainers. For each sample, 1 × 10^4 cells were analyzed on a flow cytometer through the Alexa Fluor 700 channel (ex: 633 nm, em: 710 ± 25 nm) with detailed voltages as follows: for U87MG cells: FSC, 60; SSC, 220; Alexa Fluor 700, 450 and for HEK293T cells: FSC, 100; SSC, 250; Alexa Fluor 700, 450.

Bimodal Imaging of Cell Pellets. For *in vitro* FI, U87MG cells and HEK293T cells (~1 × 10^6) were seeded in 10 cm cell culture dishes and allowed to grow for 24 h. BCGCR (10 μg/mL) in 5 mL of DMEM medium was added to U87MG and HEK293T cells. In addition, RGD-free BCGC (10 μg/mL) and RGD + BCGCR (10 μg/mL, pretreated with 10 μM cRGDfk for 1 h to block $\alpha_v\beta_3$ integrin) in 5 mL of DMEM medium were added to U87MG cells. After incubation for 2 h, the solution was removed, and these cells were rinsed by PBS once. To detach these cells, 4 mL of trypsin was added into each dish and kept for 2 min; then, 4 mL of culture medium was added to stop digestion. These cells were finally transferred into 1.5 mL tubes and centrifuged (1200 rpm, 4 min). Fluorescence images were obtained on an IVIS imaging system (ex: 675 nm, em: 720 nm). Fluorescence intensity was quantified by a region of interest (ROI) analysis using Living Image Software (4.5.2, PerkinElmer, MA, USA).

For *in vitro* MRI, U87MG cells and HEK293T cells (~2 × 10^6) were seeded in 10 cm cell culture dishes and allowed to grow for 24 h. BCGCR (10 μM Gd^{3+}) in 5 mL of DMEM medium was added to U87MG and HEK293T cells. In addition, RGD-free BCGC (10 μM Gd^{3+}) and RGD + BCGCR (10 μM Gd^{3+}, pretreated with 10 μM cRGDfk for 1 h to block $\alpha_v\beta_3$ integrin) in 5 mL of DMEM medium were added to U87MG cells. After incubation for 24 h and similar treatments mentioned above, these cells were transferred into 0.2 mL tubes and centrifuged (1200 rpm, 4 min) finally. MR images were obtained on a 1.5 T MRI system using the following parameters: T_1-weighted sequence, spin echo; TR/TE, 500/9.0 ms; image size, 128 × 256; slice thickness, 1 mm; slice number, 18; interval, 0.5 mm; field of view (FOV), 60 mm × 30 mm. The acquisition time for each scanning was 01 min 05 s. Acquired MR images were transferred into ImageJ software for quantitative analysis. Percentage signal enhancement (% SE) was calculated as the % difference ratio between the signal intensities (SI) from respective samples and those from blank samples: $\% \text{ SE} = [(\text{SI(s)} - \text{SI(b)})/\text{SI(b)} \times 100\%$.

Quantitative Analysis of the Gd Uptake in Cells. U87MG cells and HEK293T cells (~2 × 10^6) were seeded in 10 cm cell culture dishes and allowed to grow for 24 h. BCGCR (10 μM Gd^{3+}) in 5 mL of DMEM medium was added to U87MG and HEK293T cells. In addition, RGD-free BCGC (10 μM Gd^{3+}) and RGD + BCGCR (10 μM Gd^{3+}, pretreated with 10 μM cRGDfk for 1 h to block $\alpha_v\beta_3$ integrin) in 5 mL of DMEM medium were added to U87MG cells. After incubation for 24 h, these cells were rinsed, trypsinized, counted, and centrifuged. After digestion in 1 mL of aqua regia assisted by ultrasound and dilution with 4 mL of H_2O, Gd^{3+} concentrations were determined by ICP-AES; then, the average uptake of Gd in each cell was calculated.

Evaluation of Intracellular GSH Consumption. U87MG cells (~2 × 10^5) were seeded in 6-well plates and allowed to grow for 24 h. RGD-free BCGC (100 μg/mL) or BCGCR (100 μg/mL) in 2 mL of DMEM medium was added to each well and incubated for 6 h. Untreated cells were used as a control group (blank). After that, the solution was removed and rinsed carefully by PBS twice, and these cells were collected to measure intracellular GSH via a GSH assay kit.

ROS Generation Analysis. U87MG cells (~2 × 10^4) were seeded in a 48-well plate and allowed to grow for 24 h. RGD-free BCGC (100 μg/mL) or BCGCR (100 μg/mL) in 0.25 mL of DMEM medium was added to each well and incubated for 6 h. Untreated cells were used as a control group (blank). After that, the solution was removed and rinsed carefully by PBS once. DMEM medium (0.2 mL) with DCFH-DA (10 μM) was used for another 30 min of incubation; then, the cells were rinsed twice. Subsequently, 0.2 mL of fresh DMEM medium was added, and these cells were irradiated (or not) by a 980 nm laser (0.8 W/cm^2) for 5 min followed by rinsing with PBS once. Finally, the level of ROS generation from cells was evaluated using a fluorescence microscope with a GFP filter (ex: 470 ± 20 nm, em: 525 ± 25 nm).

***In Vitro* Evaluation of Cytotoxicity toward Normal HEK293T Cells (CCK-8).** HEK293T cells (~5 × 10^3) were seeded in 96-well plates and allowed to grow for 24 h. BCGCR (0, 10, 25, 50, 100, 150, and 200 μg/mL) in 0.1 mL of DMEM medium was added and incubated for 24 h. After that, the solution was removed, and these cells were rinsed with PBS once carefully. DMEM medium (0.1 mL) and 10 μL of CCK-8 solution were added to each well; then, the cells were incubated for another 2 h. The absorbance of samples (A_{sample}) at 450 nm in each well was determined using a microplate reader, while cell samples without any treatment (A_{control}) were used as a control. The *in vitro* cytotoxicity was evaluated by calculating the cell viability according to the following formula: $(A_{\text{sample}} - A_{\text{blank}})/(A_{\text{control}} - A_{\text{blank}}) \times 100\%$ (A_{blank} is the absorbance from 0.1 mL of DMEM medium and 10 μL of CCK-8 solution without cells).

***In Vitro* Evaluation of PTT and Enhanced CDT (CCK-8).** U87MG cells (~5 × 10^3) were seeded in 96-well plates and allowed to grow for 24 h. BCGC or BCGCR (0, 10, 25, 50, 100, 150, and 200 μg/mL) in 0.1 mL of DMEM medium was added and incubated for 24 h. After that, the solution was removed, and these cells were rinsed with PBS twice carefully. Fresh DMEM medium was added to each well, and these cells were irradiated by a 980 nm laser (0.8 W/cm^2) for 5 min and then allowed to grow for another 4 h. CCK-8 solution (10 μL) was added to each well; then, the cells were incubated for another 2 h. The measurement of absorbance and the subsequent calculation of cell viability were conducted as described above.

Dead/Live Cell Costaining FI Induced by PTT and Enhanced CDT. U87MG cells (~2 × 10^4) were seeded in a 48-well plate and allowed to grow for 24 h. BCGC or BCGCR (200 μg/mL) in 0.25 mL of DMEM medium was added and incubated for 24 h. Untreated cells were used as a control group (blank). After that, the solution was removed, and these cells were rinsed with PBS twice. Fresh DMEM medium was added to wells, and these cells were irradiated (or not) under a 980 nm laser (0.8 W/cm^2) for 5 min. After irradiation, these cells were allowed to continue growing for another 4 h. Fresh DMEM medium (0.2 mL) with 2 μM calcein AM and 8 μM PI was added into each well for 30 min of staining; then, cells were rinsed using PBS twice. Finally, fluorescence images were acquired using a fluorescence microscope through a GFP filter (ex: 470 ± 20 nm, em: 525 ± 25 nm) for calcein AM and a TRITC filter (ex: 545 ± 12 nm, em: 605 ± 35 nm) for PI.

Animals and Tumor Models. BALB/c female mice at the age of 5−6 weeks were purchased from Japan SLC, Inc. and used according to the regulations of Divisions of Experimental Animals, Nagoya University. A xenograft U87MG tumor model was built by s.c. injection of U87MG cells (~2 × 10^6) suspended in 100 μL of PBS into the right hind limb of mice. *In vivo* experiments were conducted when tumors with a single aspect of 5−7 mm were formed after ~4 weeks.

FI of Tumors in Mice. Three mice bearing s.c. U87MG tumors in each group were i.v. injected with BCGC or BCGCR (5 mg/kg) in 100 μL of PBS. To inhibit active recognition, mice from one group were pretreated with careful i.t. injection of cRGDfk (2 mM) in 100 μL of PBS for 1 h before i.v. injection of BCGCR. Whole-body fluorescence images were obtained before injection and 10 h, 1 day, 2 days, 4 days, and 7 days postinjection on an IVIS imaging system (ex: 675 nm, em: 720 nm). Fluorescence intensities were quantified by a region of interest (ROI) analysis, as described above.

FI of Tumor Tissue Slices. Mice bearing s.c. U87MG tumors were treated as described in the previous section and sacrificed on the second day. Tumor tissues of the mice were excised, fixed with 10% formalin, and cut into slices (thickness of 10 μm) using a vibrating blade microtome, and fluorescence images were acquired using a fluorescence microscope with a Cy5.5 filter (ex: 650 ± 22 nm, em: 720 ± 30 nm).

MRI of Tumors in Mice. Three mice bearing s.c. U87MG tumors in each group were i.v. injected with BCGC or BCGCR (20 μmol/kg Gd^{3+}) in 200 μL of PBS. To inhibit active recognition, tumors from one group were pretreated with careful i.t. injection of cRGDfk (2 mM) in 100 μL of PBS for 1 h before i.v. injection of BCGCR. MR images were acquired before injection and at 1 day, 2 days, 4 days, and 7 days postinjection using a 1.5 T MRI system with the following parameters: T_1-weighted sequence, spin echo; TR/TE, 500/9.0 ms; image size, 128 × 256; slice thickness, 1 mm; slice number, 18; interval, 0.5 mm; field of view (FOV), 60 mm × 30 mm. The acquisition time for each scan was 01 min 05 s. Acquired MR images were transferred into the ImageJ software program for a quantitative analysis. Percentage signal enhancement (% SE) was calculated as the % difference ratio between the tumor signal intensity (SI) at each time point t and the SI before injection (t_0): $\% \text{ SE}(t) = [(\text{SI}(t) - \text{SI}(t_0)]/\text{SI}(t_0) \times 100\%$.

FI of Tumors and Main Organs *Ex Vivo*. Three mice bearing s.c. U87MG tumors in each group were i.v. injected with BCGC or BCGCR (2 mg/kg) in 50 μL of PBS and sacrificed after 2 days. The tumors and main organs, including the kidneys, liver, heart, spleen, stomach, intestines, and lungs, were collected. Fluorescence images of tumors and these organs were acquired, and their intensities were quantified by a region of interest (ROI) analysis, as described above.

Biodistribution Analysis. Three mice bearing s.c. U87MG tumors in each group were i.v. injected with BCGC or BCGCR (10 mg/kg Cu^{2+}) in 200 μL of PBS followed by sacrifice and dissection after 2 days. Tumors and major organs, including the liver, kidneys, spleen, stomach, intestines, heart, and lungs, were collected and weighed, cut into small pieces, and then digested in 5 mL of aqua regia with assistance by ultrasound. The Cu^{2+} concentrations were determined by ICP-AES; then, the biodistribution % ID/g was calculated.

PTT and Enhanced CDT Evaluation of Tumors in Mice. Eight mice bearing s.c. U87MG tumors in each group were i.v. injected with 200 μL of PBS or BCGCR (5 mg/kg Cu^{2+}) dispersed in 200 μL of PBS. After 2 days, four mice among each group were irradiated by a 980 nm laser (0.8 W/cm^2) for 10 min, during which the temperature variation was monitored using an IR thermal camera. The tumor volume and body weight of each mouse were measured every three days until the 15th day. Volumes were estimated according to the formula $V = (L \times W^2)/2$, in which the length (L) and width (W) of each tumor were measured by a caliper. The relative tumor volumes of each mouse were calculated as V/V_0 (V_0 is the tumor volume before irradiation). Mice were sacrificed on the 15th day, and tumors were excised and photographed.

Histopathological Analysis. Mice bearing s.c. U87MG tumors were treated as described in the previous section and sacrificed on the second day. The tumor tissues of mice were excised, fixed with 10% formalin, cut into slices (thickness of 4 μm), and stained with hematoxylin−eosin. To examine latent side effects, major organs including the heart, liver, spleen, lungs, and kidneys from treated mice were collected on the 15th day and applied to histopathological analysis. The images were acquired using a BZ-X700 microscope with bright-field imaging.

Hematological Assay. Three healthy mice in each group were i.v. injected with 100 μL of PBS or BCGCR (5 mg/kg Cu^{2+}) dispersed in 100 μL of PBS. After 15 days, blood samples were collected for blood routine tests.

Statistical Analysis. Results are expressed as the mean ± SD unless specially stated. Statistical comparison between two groups was evaluated by Student's *t*-test. Statistical significance was considered as $P < 0.05$, which can be divided into three types, namely, * for $P < 0.05$, ** for $P < 0.01$, and *** for $P < 0.001$. All statistical calculations were conducted using OriginPro (OriginLab Corp., MA, USA).

■ ASSOCIATED CONTENT

Supporting Information

The Supporting Information is available free of charge at https://pubs.acs.org/doi/10.1021/acsami.2c06503.

> (Figures S1−S22) XPS, EDS, XRD, absorption spectra, cartoon diagrams, zeta potentials, long-term size investigation, photothermal effect, PCE evaluation, catalytic performance under different conditions, fluorescence images of tumor cells, internalization analysis, intracellular GSH consumption, cytotoxicity toward normal cells, live/dead cell costaining, fluorescence images of tumor tissue slices, T_1-weighted multislice MR images, fluorescence distribution, H&E staining of major organs, and blood routine examinations; (Tables S1 and S2) comparison of PCE and therapy conditions; (Note S1) PCE evaluation (PDF)

■ AUTHOR INFORMATION

Corresponding Authors

Hiroshi Yukawa − *Nanobio Analytical Chemistry, Biomolecular Chemistry, Department of Biomolecular Engineering, Graduate School of Engineering, Nagoya University, Nagoya 464-8603, Japan; Institute of Nano-Life-Systems, Institutes of Innovation for Future Society, Nagoya University, Nagoya 464-8603, Japan; Institute of Quantum Life Science, Quantum Life and Medical Science Directorate, National Institutes for Quantum Science and Technology, Chiba 263-8555, Japan; Nagoya University Institute for Advanced Research, Advanced Analytical and Diagnostic Imaging Center (AADIC)/Medical Engineering Unit (MEU), Nagoya 466-8550, Japan; Development of Quantum-Nano Cancer Photoimmunotherapy for Clinical Application of Refractory Cancer, Nagoya University, Nagoya 466-8550, Japan;* orcid.org/0000-0002-9352-1520; Phone: +81-52-789-5654; Email: h.yukawa@nanobio.nagoya-u.ac.jp; Fax: +81-52-789-5117

Yoshinobu Baba − *Nanobio Analytical Chemistry, Biomolecular Chemistry, Department of Biomolecular Engineering, Graduate School of Engineering, Nagoya University, Nagoya 464-8603, Japan; Institute of Nano-Life-Systems, Institutes of Innovation for Future Society, Nagoya University, Nagoya 464-8603, Japan; Institute of Quantum Life Science, Quantum Life and Medical Science Directorate, National Institutes for Quantum Science and Technology, Chiba 263-8555, Japan;* Email: babaymtt@chembio.nagoya-u.ac.jp

Authors

Minchuan Luo − *Nanobio Analytical Chemistry, Biomolecular Chemistry, Department of Biomolecular Engineering, Graduate School of Engineering, Nagoya University, Nagoya 464-8603, Japan*

Kazuhide Sato − *Institute of Nano-Life-Systems, Institutes of Innovation for Future Society, Nagoya University, Nagoya 464-8603, Japan; Nagoya University Institute for Advanced Research, Advanced Analytical and Diagnostic Imaging Center (AADIC)/Medical Engineering Unit (MEU), Nagoya 466-8550, Japan; Nagoya University Institute for Advanced Research, S-YLC, Nagoya 464-8603, Japan;* orcid.org/0000-0003-3025-088X

Makoto Tozawa − *Material Design Chemistry, Department of Materials Chemistry, Graduate School of Engineering, Nagoya University, Nagoya 464-8603, Japan*

Masato Tokunaga − *Nanobio Analytical Chemistry, Biomolecular Chemistry, Department of Biomolecular Engineering, Graduate School of Engineering, Nagoya University, Nagoya 464-8603, Japan*

Tatsuya Kameyama − *Material Design Chemistry, Department of Materials Chemistry, Graduate School of Engineering, Nagoya University, Nagoya 464-8603, Japan;* orcid.org/0000-0002-9860-6662

Tsukasa Torimoto − *Material Design Chemistry, Department of Materials Chemistry, Graduate School of Engineering, Nagoya University, Nagoya 464-8603, Japan;* orcid.org/0000-0003-0069-1916

Complete contact information is available at: https://pubs.acs.org/10.1021/acsami.2c06503

Author Contributions

M.L. and H.Y. conceived the idea and designed the project. H.Y. and Y.B. supervised, administered, and managed the project. M.L. designed and conducted most of the experiments. K.S., M.T., T.K., and T.T. conducted specific experiments. K.S., T.K., and T.T. provided expertise for the analysis of nanoparticles, *in vivo* imaging, and photothermal-intensified chemodynamic therapy of tumors. M.L., H.Y., and Y.B. wrote the paper. All the authors revised the manuscript.

Notes

The authors declare no competing financial interest.

■ ACKNOWLEDGMENTS

We thank Y. Kato for experimental assistance in *in vivo* imaging and Y. Karakida and M. Mizuno for their support in the submission of this paper. We acknowledge funding from JSPS-KAKENHI (21H05589 and 21H04663), the MEXT Quantum Leap Flagship Program (MEXT Q-LEAP, JPMXS0120330644), the SEI Group CSR Foundation, and the China Scholarship Council (CSC) (grant no. 201906920066). A part of this work was supported by the "Advanced Research Infrastructure for Materials and Nanotechnology in Japan (ARIM, Nagoya University)" of MEXT.

■ REFERENCES

(1) Aggarwal, V.; Tuli, H. S.; Varol, A.; Thakral, F.; Yerer, M. B.; Sak, K.; Varol, M.; Jain, A.; Khan, M. A.; Sethi, G. Role of Reactive

Oxygen Species in Cancer Progression: Molecular Mechanisms and Recent Advancements. *Biomolecules* **2019**, *9*, 735.

(2) Yang, B.; Chen, Y.; Shi, J. Reactive Oxygen Species (ROS)-Based Nanomedicine. *Chem. Rev.* **2019**, *119*, 4881−4985.

(3) Jin, H.; Zhu, T.; Huang, X.; Sun, M.; Li, H.; Zhu, X.; Liu, M.; Xie, Y.; Huang, W.; Yan, D. ROS-responsive Nanoparticles Based on Amphiphilic Hyperbranched Polyphosphoester for Drug Delivery: Light-triggered Size-reducing and Enhanced Tumor Penetration. *Biomaterials* **2019**, *211*, 68−80.

(4) Hu, P.; Wang, R.; Zhou, L.; Chen, L.; Wu, Q.; Han, M.; El-Toni, A. M.; Zhao, D.; Zhang, F. Near-Infrared-Activated Upconversion Nanoprobes for Sensitive Endogenous Zn^{2+} Detection and Selective On-Demand Photodynamic Therapy. *Anal. Chem.* **2017**, *89*, 3492−3500.

(5) Lan, M.; Zhao, S.; Liu, W.; Lee, C.; Zhang, W.; Wang, P. Photosensitizers for Photodynamic Therapy. *Adv. Healthcare Mater.* **2019**, *8*, 1900132.

(6) Yue, J.; Shen, Y.; Liang, L.; Cong, L.; Xu, W.; Shi, W.; Liang, C.; Xu, S. Revealing Mitochondrial Microenvironmental Evolution Triggered by Photodynamic Therapy. *Anal. Chem.* **2020**, *92*, 6081−6087.

(7) Zhang, C.; Xia, D.; Liu, J.; Huo, D.; Jiang, X.; Hu, Y. Bypassing the Immunosuppression of Myeloid-Derived Suppressor Cells by Reversing Tumor Hypoxia Using a Platelet-Inspired Platform. *Adv. Funct. Mater.* **2020**, *30*, 2000189.

(8) Yi, X.; Hu, J.; Dai, J.; Lou, X.; Zhao, Z.; Xia, F.; Tang, B. Z. Self-Guiding Polymeric Prodrug Micelles with Two Aggregation-Induced Emission Photosensitizers for Enhanced Chemo-Photodynamic Therapy. *ACS Nano* **2021**, *15*, 3026−3037.

(9) An, R.; Cheng, X.; Wei, S.; Hu, Y.; Sun, Y.; Huang, Z.; Chen, H.; Ye, D. Smart Magnetic and Fluorogenic Photosensitizer Nanoassemblies Enable Redox-Driven Disassembly for Photodynamic Therapy. *Am. Ethnol.* **2020**, *132*, 20817−20825.

(10) Zhang, L.; Wang, S.; Li, C.; Xu, L.; Cheng, H.; Zhang, X. An Adenosine Triphosphate-Responsive Autocatalytic Fenton Nanoparticle for Tumor Ablation with Self-Supplied H_2O_2 and Acceleration of Fe(III)/Fe(II) Conversion. *Nano Lett.* **2018**, *18*, 7609−7618.

(11) Lin, L.; Song, J.; Song, L.; Ke, K.; Liu, Y.; Zhou, Z.; Shen, Z.; Li, J.; Yang, Z.; Tang, W.; Niu, G.; Yang, H.; Chen, X. Simultaneous Fenton-like Ion Delivery and Glutathione Depletion by MnO_2-Based Nanoagent to Enhance Chemodynamic Therapy. *Angew. Chem., Int. Ed.* **2018**, *57*, 4902−4906.

(12) Ma, B.; Wang, S.; Liu, F.; Zhang, S.; Duan, J.; Li, Z.; Kong, Y.; Sang, Y.; Liu, H.; Bu, W.; Li, L. Self-Assembled Copper-Amino Acid Nanoparticles for in Situ Glutathione "AND" H_2O_2 Sequentially Triggered Chemodynamic Therapy. *J. Am. Chem. Soc.* **2019**, *141*, 849−857.

(13) Duesterberg, C. K.; Mylon, S. E.; Waite, T. D. pH Effects on Iron-Catalyzed Oxidation Using Fenton's Reagent. *Environ. Sci. Technol.* **2008**, *42*, 8522−8527.

(14) Brillas, E.; Baños, M. A.; Camps, S.; Arias, C.; Cabot, P. L.; Garrido, J. A.; Rodríguez, R. M. Catalytic Effect of Fe^{2+}, Cu^{2+} and UVA Light on the Electrochemical Degradation of Nitrobenzene Using an Oxygen-Diffusion Cathode. *New J. Chem.* **2004**, *28*, 314−322.

(15) Liu, Y.; Wu, J.; Jin, Y.; Zhen, W.; Wang, Y.; Liu, J.; Jin, L.; Zhang, S.; Zhao, Y.; Song, S.; Yang, Y.; Zhang, H. Copper(I) Phosphide Nanocrystals for In Situ Self-Generation Magnetic Resonance Imaging-Guided Photothermal-Enhanced Chemodynamic Synergetic Therapy Resisting Deep-Seated Tumor. *Adv. Funct. Mater.* **2019**, *29*, 1904678.

(16) Liu, C.; Wang, D.; Zhang, S.; Cheng, Y.; Yang, F.; Xing, Y.; Xu, T.; Dong, H.; Zhang, X. Biodegradable Biomimic Copper/Manganese Silicate Nanospheres for Chemodynamic/Photodynamic Synergistic Therapy with Simultaneous Glutathione Depletion and Hypoxia Relief. *ACS Nano* **2019**, *13*, 4267−4277.

(17) Zhong, X.; Wang, X.; Cheng, L.; Tang, Y.; Zhan, G.; Gong, F.; Zhang, R.; Hu, J.; Liu, Z.; Yang, X. GSH-Depleted $PtCu_3$ Nanocages for Chemodynamic- Enhanced Sonodynamic Cancer Therapy. *Adv. Funct. Mater.* **2020**, *30*, 1907954.

(18) Zhang, C.; Jing, X.; Guo, L.; Cui, C.; Hou, X.; Zuo, T.; Liu, J.; Shi, J.; Liu, X.; Zuo, X.; Li, J.; Chang, C.; Fan, C.; Wang, L. Remote Photothermal Control of DNA Origami Assembly in Cellular Environments. *Nano Lett.* **2021**, *21*, 5834−5841.

(19) Yan, H.; Chen, J.; Li, Y.; Bai, Y.; Wu, Y.; Sheng, Z.; Song, L.; Liu, C.; Zhang, H. Ultrasmall Hybrid Protein-Copper Sulfide Nanoparticles for Targeted Photoacoustic Imaging of Orthotopic Hepatocellular Carcinoma with a High Signal-To-Noise Ratio. *Biomater. Sci.* **2019**, *7*, 92−103.

(20) Zhang, L.; Gao, S.; Zhang, F.; Yang, K.; Ma, Q.; Zhu, L. Activatable Hyaluronic Acid Nanoparticle as a Theranostic Agent for Optical/Photoacoustic Image-Guided Photothermal Therapy. *ACS Nano* **2014**, *8*, 12250−12258.

(21) Shi, H.; Sun, Y.; Yan, R.; Liu, S.; Zhu, L.; Liu, S.; Feng, Y.; Wang, P.; He, J.; Zhou, Z.; Ye, D. Magnetic Semiconductor Gd-Doping CuS Nanoparticles as Activatable Nanoprobes for Bimodal Imaging and Targeted Photothermal Therapy of Gastric Tumors. *Nano Lett.* **2019**, *19*, 937−947.

(22) Jiang, W.; Zhang, H.; Wu, J.; Zhai, G.; Li, Z.; Luan, Y.; Garg, S. CuS@MOF-Based Well-Designed Quercetin Delivery System for Chemo-Photothermal Therapy. *ACS Appl. Mater. Interfaces* **2018**, *10*, 34513−34523.

(23) Hu, J.; Cheng, Y.; Zhang, X. Recent Advances in Nanomaterials for Enhanced Photothermal Therapy of Tumors. *Nanoscale* **2018**, *10*, 22657−22672.

(24) Sun, H.; Zhang, Q.; Li, J.; Peng, S.; Wang, X.; Cai, R. Near-Infrared Photoactivated Nanomedicines for Photothermal Synergistic Cancer Therapy. *Nano Today* **2021**, *37*, 101073.

(25) Li, X.; Zhang, D.; Yin, C.; Lu, G.; Wan, Y.; Huang, Z.; Tan, J.; Li, S.; Luo, J.; Lee, C. A Diradicaloid Small Molecular Nanotheranostic with Strong Near-Infrared Absorbance for Effective Cancer Photoacoustic Imaging and Photothermal Therapy. *ACS Appl. Mater. Interfaces* **2021**, *13*, 15983−15991.

(26) Zhang, R.; Wang, Z.; Xu, L.; Xu, Y.; Lin, Y.; Zhang, Y.; Sun, Y.; Yang, G. Rational Design of a Multifunctional Molecular Dye with Single Dose and Laser for Efficiency NIR-II Fluorescence/Photoacoustic Imaging Guided Photothermal Therapy. *Anal. Chem.* **2019**, *91*, 12476−12483.

(27) Sun, H.; Zhang, Y.; Chen, S.; Wang, R.; Chen, Q.; Li, J.; Luo, Y.; Wang, X.; Chen, H. Photothermal Fenton Nanocatalysts for Synergetic Cancer Therapy in the Second Near-Infrared Window. *ACS Appl. Mater. Interfaces* **2020**, *12*, 30145−30154.

(28) Liu, C.; Tang, H.; Zheng, X.; Yang, D.; Zhang, Y.; Zhang, J.; Kankala, R. K.; Wang, S.; Liu, G.; Chen, A. Near-Infrared-Activated Lysosome Pathway Death Induced by ROS Generated from Layered Double Hydroxide-Copper Sulfide Nanocomposites. *ACS Appl. Mater. Interfaces* **2020**, *12*, 40673−40683.

(29) Wen, R.; Lv, X.; Yang, T.; Li, Y.; Tang, Y.; Bai, X.; Ke, H.; Shen, J.; Chen, H. Albumin Nanoreactor-templated Synthesis of Gd_2O_3/CuS Hybrid Nanodots for Cancer Theranostics. *Sci. China Mater.* **2017**, *60*, 554−562.

(30) Yang, W.; Guo, W.; Le, W.; Lv, G.; Zhang, F.; Shi, L.; Wang, X.; Wang, J.; Wang, S.; Chang, J.; Zhang, B. Albumin-Bioinspired Gd:CuS Nanotheranostic Agent for In vivo Photoacoustic/Magnetic Resonance Imaging-Guided Tumor-Targeted Photothermal Therapy. *ACS Nano* **2016**, *10*, 10245−10257.

(31) Tanford, C.; Buzzell, J. G.; Rands, D. G.; Swanson, S. A. The Reversible Expansion of Bovine Serum Albumin in Acid Solutions. *J. Am. Chem. Soc.* **1955**, *77*, 6421−6428.

(32) Yukawa, H.; Baba, Y. In vivo Fluorescence Imaging and the Diagnosis of Stem Cells Using Quantum Dots for Regenerative Medicine. *Anal. Chem.* **2017**, *89*, 2671−2681.

(33) Yukawa, H.; Watanabe, M.; Kaji, N.; Okamoto, Y.; Tokeshi, M.; Miyamoto, Y.; Noguchi, H.; Baba, Y.; Hayashi, S. Monitoring Transplanted Adipose Tissue-Derived Stem Cells Combined with Heparin in the Liver by Fluorescence Imaging Using Quantum Dots. *Biomaterials* **2012**, *33*, 2177−2186.

https://doi.org/10.1021/acsami.2c06503
ACS Appl. Mater. Interfaces 2022, 14, 34365−34376

(34) Zhang, C.; Yuan, Y.; Wu, K.; Wang, Y.; Zhu, S.; Shi, J.; Wang, L.; Li, Q.; Zuo, X.; Fan, C.; Chang, C.; Li, J. Driving DNA Origami Assembly with a Terahertz Wave. *Nano Lett.* **2022**, *22*, 468−475.

(35) Li, W.; Wang, C.; Lv, H.; Wang, Z.; Zhao, M.; Liu, S.; Gou, L.; Zhou, Y.; Li, J.; Zhang, J.; Li, L.; Wang, Y.; Lou, P.; Wu, L.; Zhou, L.; Chen, Y.; Lu, Y.; Cheng, J.; Han, Y.; Cao, Q.; Huang, W.; Tong, N.; Fu, X.; Liu, J.; Zheng, X.; Berggren, P. A DNA Nanoraft-Based Cytokine Delivery Platform for Alleviation of Acute Kidney Injury. *ACS Nano* **2021**, *15*, 18237−18249.

(36) Nishinaga, Y.; Sato, K.; Yasui, H.; Taki, S.; Kazuomi, T.; Shimizu, M.; Endo, R.; Koike, C.; Kuramoto, N.; Nakamura, S.; Fukui, T.; Yukawa, H.; Baba, Y.; Kaneko, M. K.; Chen-Yoshikawa, T. F.; Kobayashi, H.; Kato, Y.; Hasegawa, Y. Targeted Phototherapy for Malignant Pleural Mesothelioma: Near-Infrared Photoimmunotherapy Targeting Podoplanin. *Cell* **2020**, *9*, 1019.

(37) Wahsner, J.; Gale, E. M.; Rodríguez-Rodríguez, A.; Caravan, P. Chemistry of MRI Contrast Agents: Current Challenges and New Frontiers. *Chem. Rev.* **2019**, *119*, 957−1057.

(38) Caspani, S.; Magalhães, R.; Araújo, J. P.; Sousa, C. T. Magnetic Nanomaterials as Contrast Agents for MRI. *Materials* **2020**, *13*, 2586.

(39) Zhou, Z.; Deng, H.; Yang, W.; Wang, Z.; Lin, L.; Munasinghe, J.; Jacobson, O.; Liu, Y.; Tang, L.; Ni, Q.; Kang, F.; Liu, Y.; Niu, G.; Bai, R.; Qian, C.; Song, J.; Chen, X. Early Stratification of Radiotherapy Response by Activatable Inflammation Magnetic Resonance Imaging. *Nat. Commun.* **2020**, *11*, 3032.

(40) Wu, B.; Lu, S.; Yu, H.; Liao, R.; Li, H.; Zafitatsimo, B. V. L.; Li, Y.; Zhang, Y.; Zhu, X.; Liu, H.; Xu, H.; Huang, S.; Cheng, Z. Gadolinium-chelate Functionalized Bismuth Nanotheranostic Agent for In Vivo MRI/CT/PAI Imaging-guided Photothermal Cancer Therapy. *Biomaterials* **2018**, *159*, 37−47.

(41) Danhier, F.; Breton, A. L.; Préat, V. RGD-Based Strategies To Target Alpha(v) Beta(3) Integrin in Cancer Therapy and Diagnosis. *Mol. Pharmaceutics* **2012**, *9*, 2961−2973.

(42) Temming, K.; Schiffelers, R. M.; Molema, G.; Kok, R. J. RGD-based Strategies for Selective Delivery of Therapeutics and Imaging Agents to the Tumor Vasculature. *Drug Resist. Update* **2005**, *8*, 381−402.

(43) Herborn, C. U.; Honold, E.; Wolf, M.; Kemper, J.; Kinner, S.; Adam, G.; Barkhausen, J. Clinical Safety and Diagnostic Value of the Gadolinium Chelate Gadoterate Meglumine (Gd-DOTA). *Invest. Radiol.* **2007**, *42*, 58−62.

(44) Kuang, Y.; Cao, Y.; Liu, M.; Zu, G.; Zhang, Y.; Zhang, Y.; Pei, R. Geometrical Confinement of Gadolinium Oxide Nanoparticles in Poly(ethylene glycol)/Arginylglycylaspartic Acid-Modified Mesoporous Carbon Nanospheres as an Enhanced T_1 Magnetic Resonance Imaging Contrast Agent. *ACS Appl. Mater. Interfaces* **2018**, *10*, 26099−26107.

(45) Wang, L.; Lin, H.; Ma, L.; Sun, C.; Huang, J.; Li, A.; Zhao, T.; Chen, Z.; Gao, J. Geometrical Confinement Directed Albumin-Based Nanoprobes as Enhanced T_1 Contrast Agents for Tumor Imaging. *J. Mater. Chem. B* **2017**, *5*, 8004−8012.

(46) Chen, X.; Conti, P. S.; Moats, R. A. In vivo Near-Infrared Fluorescence Imaging of Integrin $\alpha_v\beta_3$ in Brain Tumor Xenografts. *Cancer Res.* **2004**, *64*, 8009−8014.

(47) Robinson, J. T.; Tabakman, S. M.; Liang, Y.; Wang, H.; Casalongue, H. S.; Vinh, D.; Dai, H. Ultrasmall Reduced Graphene Oxide with High Near-Infrared Absorbance for Photothermal Therapy. *J. Am. Chem. Soc.* **2011**, *133*, 6825−6831.

(48) Tang, Z.; Zhang, H.; Liu, Y.; Ni, D.; Zhang, H.; Zhang, J.; Yao, Z.; He, M.; Shi, J.; Bu, W. Antiferromagnetic Pyrite as the Tumor Microenvironment-Mediated Nanoplatform for Self-Enhanced Tumor Imaging and Therapy. *Adv. Mater.* **2017**, *29*, 1701683.